Boosting photocatalytic hydrogen evolution via intrinsic electric fields in 2D Janus $AlXY_2$ (X = Ga, In; Y = S, Se, Te) monolayers

Zafer, Talha; Khossossi, Nabil; Dey, Poulumi

DOI
10.1016/j.apsadv.2025.100851

Publication date
2025

Document Version
Final published version

Published in
Applied Surface Science Advances

Applied Surface Science Advances 30 (2025) 100851

Contents lists available at ScienceDirect

Applied Surface Science Advances

journal homepage: www.sciencedirect.com/journal/applied-surface-science-advances

Full length article

Boosting photocatalytic hydrogen evolution via intrinsic electric fields in 2D Janus $AlXY_2$ (X = Ga, In; Y = S, Se, Te) monolayers

Talha Zafer [a,b,*], Nabil Khossossi [c], Poulumi Dey [a]

[a] Department of Materials Science and Engineering, Faculty of Mechanical Engineering, Delft University of Technology, 2628 CD Delft, The Netherlands
[b] Vocational School of Health Services, Sakarya University, 54050, Sakarya, Turkey
[c] DIFFER — Dutch Institute for Fundamental Energy Research, 5612 AJ Eindhoven, The Netherlands

ARTICLE INFO

Keywords:
2D layered III–VI metal chalcogenides
Hydrogen production
Photocatalytic water splitting
First-principle calculations

ABSTRACT

Photocatalytic water splitting represents a promising approach for sustainable hydrogen production, with two-dimensional Janus materials offering unique advantages through intrinsic electric fields that enhance charge separation. We present a comprehensive first-principles investigation of Janus $AlXY_2$ (X = Ga, In; Y = S, Se, Te) monolayers using density functional theory and ab initio molecular dynamics simulations. All six systems exhibit excellent structural, thermal, and mechanical stability with HSE06 bandgaps of 2.029–2.969 eV suitable for UV-light absorption. The asymmetric structure generates strong intrinsic electric fields of 5.391–6.437 V perpendicular to the monolayer plane, significantly enhancing photogenerated charge carrier separation. While pristine monolayers show poor hydrogen evolution reaction (HER) activity with Gibbs free energies of 1.937–2.371 eV, strategic introduction of metal vacancies dramatically improves performance, reducing ΔG_H values to −0.371 to +0.607 eV and approaching optimal catalytic conditions. These findings demonstrate the potential of defect-engineered 2D Janus $AlXY_2$ materials for efficient photocatalytic hydrogen production.

1. Introduction

Increasing global energy demand and environmental concerns have driven extensive research into sustainable and clean energy alternatives to fossil fuels [1,2]. Hydrogen, as a carbon-free energy carrier with high energy density, represents one of the most promising candidates for future energy systems [3,4]. Among various hydrogen production methods, photocatalytic water splitting has emerged as an attractive approach due to its potential to directly convert abundant solar energy into chemical energy without carbon emissions [5,6]. However, the development of efficient photocatalysts remains a key challenge for practical implementation. An ideal photocatalyst requires: (i) a suitable band gap for effective solar light absorption, (ii) band edge positions aligned with water redox potentials, (iii) efficient charge carrier separation and transport to reduce recombination, and (iv) numerous active sites for surface reactions [7,8]. Traditional photocatalysts such as TiO_2 and other metal oxides often suffer from wide band gaps, rapid charge carrier recombination, and insufficient active sites for catalytic reactions [9,10].

To address these limitations, two-dimensional (2D) materials have attracted considerable attention in photocatalysis research due to their unique properties, including high specific surface areas, abundant active sites, and tunable electronic structures [11,12]. Following the successful exfoliation of graphene, numerous 2D materials have been explored for photocatalytic applications, including transition metal dichalcogenides (TMDs), metal oxides, nitrides, and carbon nitride [13–16]. Despite significant progress, most conventional 2D materials face limitations in photocatalytic efficiency due to rapid charge carrier recombination and suboptimal band edge positions [17,18]. A breakthrough in this field came with the emergence of Janus structures, a novel class of 2D materials characterized by their asymmetric composition and broken mirror symmetry [19,20]. Named after the two-faced Roman god, Janus 2D materials feature different atomic species on their top and bottom surfaces, creating an inherent structural asymmetry. This asymmetry induces an intrinsic out-of-plane electric field, which can significantly enhance photocatalytic performance by facilitating the separation of photogenerated electron–hole pairs and reducing recombination losses [21,22].

The first experimental realization of a 2D Janus structure was achieved with MoSSe monolayer in 2017 through chemical vapor deposition, synthesized by either selenization of MoS_2 or sulfurization of

* Corresponding author at: Department of Materials Science and Engineering, Faculty of Mechanical Engineering, Delft University of Technology, 2628 CD Delft, The Netherlands.
E-mail address: t.zafer@tudelft.nl (T. Zafer).

https://doi.org/10.1016/j.apsadv.2025.100851
Received 20 June 2025; Received in revised form 3 September 2025; Accepted 8 September 2025
Available online 18 September 2025

$MoSe_2$ monolayers [23]. This breakthrough has stimulated extensive research into various Janus TMDs, including WSSe, MoSTe, and WSeTe, revealing their promising properties for photocatalytic applications [24,25]. Ju et al. demonstrated that Janus WSSe monolayers exhibit superior photocatalytic performance compared to their parent materials (WS_2 and WSe_2) due to the enhanced charge carrier separation enabled by the intrinsic electric field [24]. Beyond TMDs, another important family of Janus 2D materials comprises Group-III metal chalcogenides with the chemical formula M_2XY (M = Al; X = Ga, In; Y = S, Se, Te; X ≠ Y) which represent promising candidates due to their unique electronic, optical, and catalytic properties arising from their intrinsic dipole moments and asymmetric electron distribution [26,27]. Among them, Janus Ga_2SSe and In_2SSe monolayers have been theoretically predicted to exhibit promising photocatalytic properties for water splitting [28,29], while 2D Janus Al_2XY (X = Ga, In; Y = S, Se, Te) monolayers demonstrate suitable band gaps and favorable band edge positions for photocatalytic applications [30,31]. Most recently, Wan et al. have systematically investigated the photocatalytic properties of pristine Janus XYZ_2 monolayers reporting band gaps of 1.60–3.11 eV and enhanced charge separation driven by built-in electric fields, making them suitable for water splitting across various pH ranges [32].

Building on these insights, we present a comprehensive investigation of 2D Janus group-III metal chalcogenides ($AlXY_2$, where X = Ga, In and Y = S, Se, Te) as potential photocatalysts for water splitting, with a particular focus on hydrogen evolution reactions (HER). Through systematic density functional theory (DFT) calculations, we explore their structural stability, electronic properties, and band edge alignments relative to water redox potentials. Our analysis reveals that the intrinsic electric field generated by the asymmetric Janus structure fundamentally enhances photocatalytic performance by promoting efficient charge carrier separation and creating optimal band edge positions for both hydrogen and oxygen evolution reactions. The built-in electric field not only reduces electron–hole recombination rates but also modulates the work function and surface reactivity, leading to improved catalytic efficiency. Furthermore, we systematically investigate how point defects, particularly metal vacancies, modify the electronic structure and catalytic activity of these materials. Our defect analysis demonstrates that controlled metal vacancy introduction can serve as an effective strategy for fine-tuning the electronic properties and enhancing the density of active sites for hydrogen evolution. Our findings reveal that these 2D Janus group-III metal chalcogenides exhibit exceptional characteristics for efficient photocatalytic hydrogen production, with several compositions showing superior performance metrics compared to conventional photocatalysts, offering new opportunities for the development of high-performance photocatalysts for clean energy applications.

2. Results and discussion

2.1. Geometry and structural stability

The 2D Janus $AlXY_2$ (X = Ga, In; Y = S, Se, Te) monolayers adopt a hexagonal crystal structure with space group P3m1 (No. 156), as illustrated in Fig. 1. The structure exhibits a four-layer atomic arrangement where each unit cell contains one aluminum atom, one group-III metal atom (Ga or In), and two chalcogen atoms, with the metal atoms forming the inner bilayer sandwiched between identical chalcogen layers on both surfaces. This asymmetric metal distribution—with Al and X occupying distinct sublattices within the central bilayer—creates the characteristic Janus geometry that distinguishes these materials from conventional symmetric 2D systems. The resulting structural asymmetry fundamentally breaks the vertical mirror symmetry, establishing a permanent electric dipole moment perpendicular to the basal plane and generating an intrinsic built-in electric field of several V/nm that drives efficient spatial separation of photogenerated electron–hole pairs, thereby significantly enhancing photocatalytic efficiency by suppressing charge recombination processes.

The structural parameters of all six $AlXY_2$ systems ($AlGaS_2$, $AlGaSe_2$, $AlGaTe_2$, $AlInS_2$, $AlInSe_2$, and $AlInTe_2$) exhibit systematic trends that directly correlate with their electronic and catalytic properties. The optimized lattice parameters and key structural properties are summarized in Table S1. The lattice constants ($a = b$) systematically increase with the atomic radius of the chalcogen atoms, ranging from 3.592 Å for $AlGaS_2$ to 4.220 Å for $AlInTe_2$, reflecting the progressive expansion of the crystal lattice. Similarly, the bond lengths between metal atoms (Al-X) and metal-chalcogen bonds (Al-Y, X-Y) follow predictable trends based on atomic radii, with these geometric variations playing a critical role in determining the electronic band structure and surface reactivity for hydrogen evolution. The monolayer thickness (h), defined as the distance between the outermost chalcogen atoms, ranges from 4.673 Å for $AlGaS_2$ to 5.360 Å for $AlInTe_2$, with this structural parameter directly influencing the strength of the built-in electric field and the resulting photocatalytic efficiency.

Thermodynamic stability assessment through formation energy calculations demonstrates that all six $AlXY_2$ systems are energetically favorable for experimental synthesis and possess sufficient thermodynamic driving force for stable formation. The formation energy (E_f) per atom was calculated using the equation [33]:

$$E_{\mathrm{f}} = \frac{E(\mathrm{AlXY_2}) - [E(\mathrm{Al}) + E(\mathrm{X}) + 2E(\mathrm{Y})]}{4}, \quad (1)$$

where $E(AlXY_2)$ represents the total energy of the fully relaxed $AlXY_2$ monolayer, and E(Al), E(X), and E(Y) are the energies of isolated Al, X (Ga or In), and Y (S, Se, Te) atoms in their ground state configurations, respectively. The denominator of 4 accounts for the total number of atoms in the formula unit, providing the formation energy per atom for direct comparison across different compositions. All systems exhibit substantially negative formation energies (Table S1), ranging from −0.360 eV for $AlGaSe_2$ to −0.894 eV for $AlGaS_2$, unambiguously confirming their thermodynamic stability and synthetic feasibility. Notably, sulfur-containing compounds demonstrate the highest thermodynamic stability (−0.894 eV for $AlGaS_2$ and −0.709 eV for $AlInS_2$), attributed to the formation of stronger Al-S and X-S bonds arising from sulfur's smaller atomic radius (1.04 Å) and higher electronegativity (2.58) compared to selenium and tellurium. This enhanced bonding stability not only facilitates synthesis but also suggests superior structural integrity under photocatalytic operating conditions, making sulfur-based systems particularly attractive for practical hydrogen evolution applications.

2.2. Lattice dynamic stability and thermal stability

Dynamic stability assessment through comprehensive phonon dispersion analysis confirms the structural viability of all six $AlXY_2$ systems for experimental synthesis and long-term photocatalytic operation. Phonon dispersion calculations performed using the finite displacement method [34] reveal the absence of imaginary frequencies throughout the entire Brillouin zone for all systems, providing unambiguous confirmation of their dynamic stability—a critical prerequisite for practical device applications (Figure S1). The calculated phonon spectra along high-symmetry paths (Γ-M-K-Γ) exhibit characteristic features that directly impact their photocatalytic performance. All systems display three acoustic branches, including the out-of-plane acoustic (ZA) mode with the quadratic dispersion typical of 2D materials. A systematic decrease in vibrational frequencies occurs with increasing chalcogen atomic mass, with the highest optical modes reaching 14 THz for $AlGaS_2$, 12 THz for $AlGaSe_2$, and 11 THz for $AlGaTe_2$. This mass-dependent frequency scaling directly influences electron–phonon coupling strength and thermal transport properties, both crucial factors determining photocatalytic efficiency through their effects on charge carrier lifetimes and heat dissipation during catalytic reactions.

The inherent Janus asymmetry fundamentally modifies the vibrational characteristics compared to conventional symmetric 2D materials [35,36], creating distinct phonon polarization patterns that can

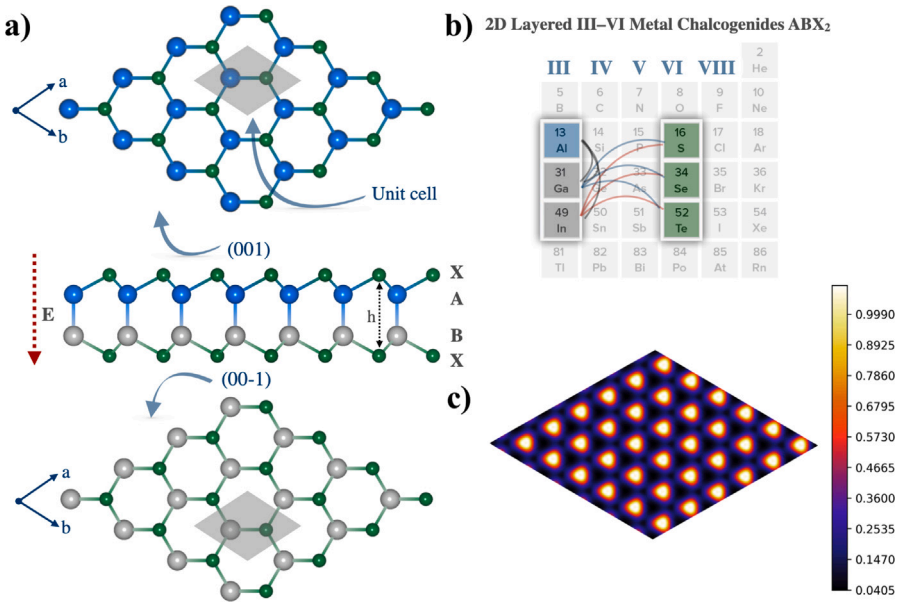

Fig. 1. (a) Fully relaxed structure of AlXY2 monolayer with top view and side view (b) Periodic table highlighting the constituent elements: Al (group III), Ga/In (group III), and S/Se/Te (group VI chalcogens).(c) Charge density distribution map.

influence charge carrier scattering mechanisms. The separation between acoustic and optical phonon branches becomes progressively more pronounced in heavier chalcogen systems, reflecting the increased mass contrast within the unit cell and potentially affecting the electron–phonon interaction strength that governs charge carrier mobility and recombination rates. Notably, the acoustic modes near the Γ point exhibit clear anisotropic behavior, with phonon group velocities showing directional dependence that correlates with the elastic anisotropy of these materials. Thermal stability validation through extensive ab initio molecular dynamics (AIMD) simulations demonstrates exceptional structural robustness under realistic operating conditions. Simulations conducted at 300 K and 600 K over 10 ps trajectories using 1 fs timesteps with appropriate thermostats reveal remarkable stability across the entire series. Representative systems $AlGaS_2$ and $AlGaSe_2$ exhibit minimal energy fluctuations (±30 meV/atom) and maintain stable temperature profiles throughout the simulation period, while the remaining systems ($AlGaTe_2$, $AlInS_2$, $AlInSe_2$, and $AlInTe_2$) demonstrate comparable thermal stability (Figure S2).

To evaluate the stability of catalytically active defective structures, additional AIMD simulations were performed on vacancy-containing $AlXY_2$ systems. The results demonstrate that single metal vacancies – which serve as active sites for hydrogen adsorption and evolution – do not compromise the overall thermal stability of the host lattice. While localized atomic fluctuations around defect sites exhibit enhanced amplitudes compared to pristine regions, the fundamental crystallographic framework remains intact throughout extended simulation periods. This finding validates the practical viability of defect-engineered $AlXY_2$ materials for sustained high-performance hydrogen evolution under realistic operating conditions, confirming that the enhanced catalytic activity achieved through vacancy engineering does not come at the expense of structural stability. These results establish that all six $AlXY_2$ systems possess the thermal resilience required for sustained photocatalytic operation under both ambient and elevated temperature conditions typical of solar-driven hydrogen production processes.

2.3. Mechanical properties

Comprehensive mechanical characterization reveals that the 2D Janus $AlXY_2$ monolayers possess excellent mechanical stability and tunable elastic properties suitable for diverse technological applications. The mechanical properties were investigated through elastic constant calculations, which provide fundamental insights into their structural integrity, deformation resistance, and potential for strain engineering in photocatalytic devices. For 2D hexagonal structures, the elastic tensor is characterized by three independent elastic constants: C_{11}, C_{12}, and C_{66}, as presented in Table 1. All six systems satisfy the necessary mechanical stability criteria ($C_{11} > 0$, $C_{66} > 0$, and $C_{11} > C_{12}$), confirming their structural integrity under mechanical stress and validating their suitability for practical device applications. The layer modulus ($\gamma = (C_{11}+C_{12})/2$), which quantifies resistance to area changes under biaxial stress, exhibits a systematic decrease from 76.20 N/m for $AlGaS_2$ to 47.63 N/m for $AlInTe_2$, directly correlating with the progressive weakening of interatomic bonds as atomic radii increase and electronegativity decreases across the series.

The in-plane Young's modulus (Y_{2D}) demonstrates similar compositional trends, systematically decreasing from 107.554 N/m for $AlGaS_2$ to 67.532 N/m for $AlInTe_2$, reflecting the fundamental relationship between chemical bonding strength and mechanical stiffness. These values are competitive with other technologically relevant 2D materials such as phosphorene, while remaining more flexible than ultra-stiff materials like graphene and MoS_2 [37–39], positioning them favorably for applications requiring moderate mechanical flexibility combined with structural stability. The calculated Poisson's ratios (ν) range from 0.271 to 0.325, falling within the typical range for 2D semiconductors and indicating balanced elastic response under uniaxial stress [40]. Notably, the Janus asymmetry does not significantly compromise the mechanical isotropy, as evidenced by the nearly circular polar diagrams of Young's modulus and Poisson's ratio (Fig. 2), suggesting uniform mechanical response across different crystallographic directions despite the structural asymmetry.

The directional analysis reveals remarkably isotropic mechanical behavior, with polar diagrams showing nearly circular patterns for both Young's modulus and Poisson's ratio across all compositions. This mechanical isotropy, despite the inherent structural asymmetry of Janus materials, indicates that the out-of-plane electric field responsible for enhanced photocatalytic performance does not compromise the in-plane mechanical uniformity. The systematic compositional effects are clearly evident: Ga→ In substitution (involving larger atomic radius and lower electronegativity) consistently reduces mechanical stiffness, while S→ Te progression similarly decreases elastic moduli due to weaker bonding interactions. These tunable mechanical properties enable targeted applications: stiffer compositions like $AlGaS_2$ are ideal

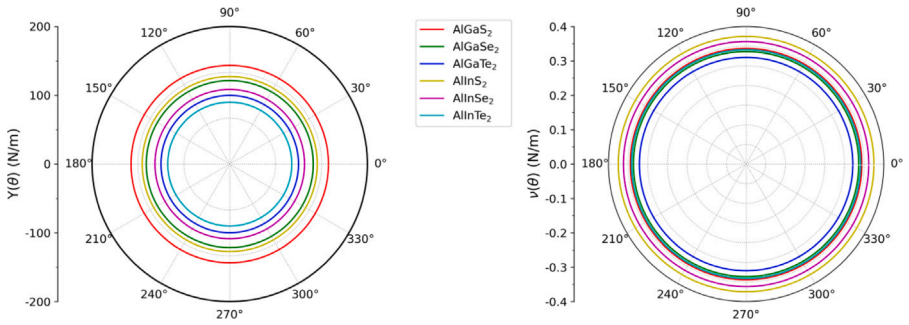

Fig. 2. Polar diagrams of in-plane Young's modulus $Y(\theta)$ and Poisson's ratio $\nu(\theta)$ along an arbitrary in-plane direction θ (angle relative to the x-direction) for Janus chalcogenide $AlXY_2$ (X: Ga, In; Y: S, Se, Te) monolayers.

Table 1
Elastic constants (C_{ij}, N/m), Layer modulus (γ, N/m), Young's modulus (Y_{2D}, N/m), Poisson's ratio (ν) of six 2D Janus chalcogenide $AlXY_2$ monolayers.

Materials	C_{11} (N/m)	C_{12} (N/m)	C_{66} (N/m)	γ (N/m)	Y_{2D} (N/m)	ν
$AlGaS_2$	117.749	34.647	41.551	76.20	107.554	0.294
$AlGaSe_2$	99.112	28.376	35.368	63.74	90.988	0.286
$AlGaTe_2$	80.879	21.940	29.469	51.41	74.927	0.271
$AlInS_2$	106.606	34.628	35.989	70.62	95.358	0.325
$AlInSe_2$	90.226	28.134	31.046	59.18	81.454	0.312
$AlInTe_2$	73.782	21.474	26.154	47.63	67.532	0.291

for structural reinforcement and high-stress environments, while more flexible systems like $AlInTe_2$ are suitable for flexible electronics and strain-sensitive applications. The combination of mechanical stability, tunable stiffness, and directional uniformity makes these materials particularly attractive for strain-engineered photocatalytic devices where controlled mechanical deformation can be used to optimize electronic band structures for enhanced hydrogen evolution performance.

2.4. Electronic properties and chemical bonding analysis

The computed electronic structure of 2D Janus $AlXY_2$ monolayers reveals optimal characteristics for photocatalytic water splitting, combining suitable band gaps with intrinsic charge separation mechanisms that address the fundamental challenge of rapid electron–hole recombination in conventional photocatalysts. Electronic properties were systematically investigated using both PBE and HSE06 functionals, with the hybrid HSE06 functional providing more accurate band gap values by correcting the well-known DFT underestimation of semiconductor band gaps through inclusion of exact exchange interactions. The calculated band structures (Fig. 3) reveal indirect band gap semiconductors with strategically positioned band edges: the conduction band minimum (CBM) consistently appears near the M point, while the valence band maximum (VBM) undergoes a systematic shift from the K-Γ region for sulfur-containing compounds to the Γ point for selenium and tellurium systems. This indirect nature facilitates longer charge carrier lifetimes compared to direct gap materials, as the momentum mismatch reduces radiative recombination rates and enhances the probability of charge carriers reaching catalytically active surface sites. The HSE06 band gaps span from 2.029 eV ($AlInTe_2$) to 2.969 eV ($AlGaS_2$), systematically decreasing with increasing chalcogen size and decreasing with Ga→ In substitution, reflecting the progressive weakening of metal-chalcogen bonding interactions and reduction in orbital overlap as atomic radii increase.

Orbital-resolved band structure analysis reveals highly favorable characteristics for photocatalytic charge separation and surface reactivity. The projected density of states (Figure S4-5) demonstrates that the VBM originates predominantly from chalcogen p-orbitals, while the CBM involves hybridized metal and chalcogen p-states, creating spatial charge separation upon photoexcitation where holes localize primarily on chalcogen atoms while electrons distribute across both metal and chalcogen sites. This orbital distribution is particularly advantageous for water splitting, as the hole-rich chalcogen surfaces can facilitate oxygen evolution reactions while the electron-enriched metal sites promote hydrogen evolution, effectively creating spatially separated redox active regions that minimize back-reactions and enhance overall catalytic efficiency. The electronic structure also exhibits strong covalent-ionic character, as evidenced by comprehensive Bader charge analysis (Table 2), which reveals substantial charge transfer from metal to chalcogen atoms with Al consistently donating 0.322–1.017 |e| and chalcogens accepting electrons according to their electronegativity hierarchy.

The calculated electrostatic potential differences ($\Delta\phi$) range from 5.391 V for $AlGaTe_2$ to 6.437 V for $AlGaS_2$, corresponding to electric field strengths of several V/nm that create powerful driving forces for charge carrier separation. This intrinsic electric field acts as a permanent internal bias that spatially separates photogenerated electrons and holes, dramatically reducing recombination rates and extending charge carrier lifetimes for enhanced surface reaction kinetics. The electric dipole moments range from 0.154 D to 0.408 D, with In-containing systems showing systematically higher values due to greater asymmetry in charge distribution, indicating stronger built-in fields that could translate to superior photocatalytic performance. While the calculated HSE06 band gaps of 2.029–2.969 eV correspond primarily to UV-blue light absorption, these values are comparable to established photocatalysts like TiO_2 and fall within the range suitable for solar-driven water splitting. The exceptionally strong intrinsic electric fields (5.391–6.437 V) provide significant advantages for addressing charge recombination—often the primary limiting factor in photocatalytic efficiency. Future optimization strategies could include band gap engineering through alloying, strain application, or heterostructure formation to extend visible light absorption while preserving the beneficial Janus-induced charge separation properties, potentially yielding photocatalysts with both optimal light harvesting and superior charge dynamics.

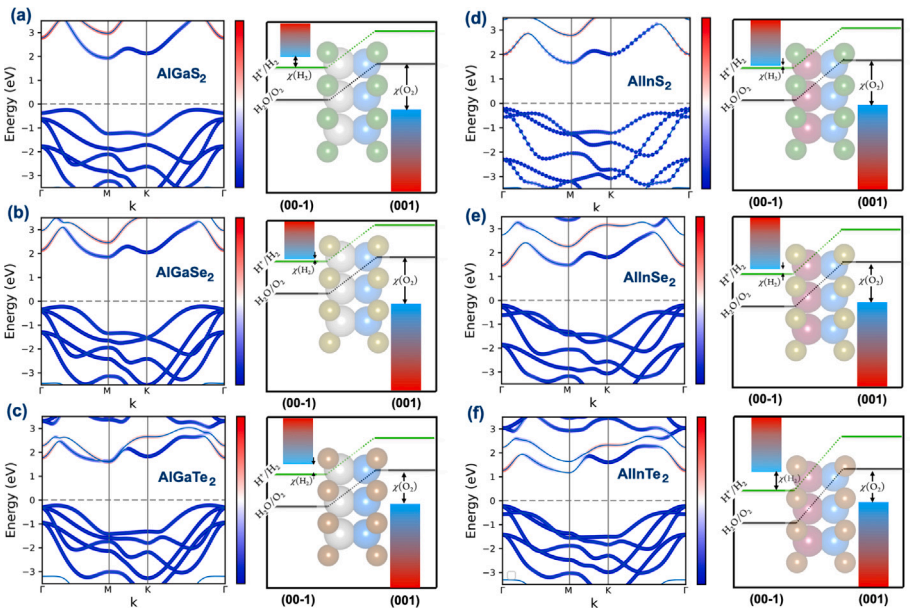

Fig. 3. Electronic Properties and Band Alignments of 2D Janus $AlXY_2$ Monolayers (a–f) Band structures (left panels) and band edge positions relative to water redox potentials (right panels) for $AlGaS_2$, $AlGaSe_2$, $AlGaTe_2$, $AlInS_2$, $AlInSe_2$, and $AlInTe_2$, respectively. The dashed gray line represents the Fermi level (set to 0 eV). The green horizontal lines indicate the redox potentials for hydrogen evolution (H^+/H_2) and gray horizontal lines for oxygen evolution (H_2O/O_2). Red–blue color gradients represent the electrostatic potential difference across the monolayers, illustrating the intrinsic electric field that enhances charge carrier separation.

Table 2
Electronic properties and charge states of 2D Janus $AlXY_2$ monolayers (X = Ga/In, Y = S/Se/Te). E_g^{PBE} and E_g^{HSE06} are band gaps from PBE and HSE06 functionals (eV); μ is the electric dipole moment (D); $\Delta\phi$ is the electrostatic potential difference (V); Q_{Al}, Q_X, Q_Y are average Bader charges on Al, X, and Y atoms (e).

$AlXY_2$	Electronic properties				Average Charge State		
	E_g^{PBE}	E_g^{HSE-06}	μ	$\Delta\phi$	Q_{Al}	Q_X	Q_Y
$AlGaS_2$	2.161	2.969	0.236	6.437	−1.017	−0.413	+0.715
$AlGaSe_2$	2.068	2.824	0.194	6.003	−0.765	−0.269	+0.517
$AlGaTe_2$	1.816	2.507	0.154	5.391	−0.630	+0.005	+0.312
$AlInS_2$	1.928	2.622	0.408	6.402	−0.322	−0.468	+0.395
$AlInSe_2$	1.706	2.390	0.308	5.703	−0.608	−0.364	+0.486
$AlInTe_2$	1.439	2.029	0.219	5.603	−0.371	−0.268	+0.319

2.5. Defect-mediated hydrogen evolution

The electronic structure analysis revealed a fundamental limitation of pristine 2D Janus $AlXY_2$ monolayers for hydrogen evolution catalysis, despite their favorable charge separation properties, the pristine surfaces exhibit prohibitively weak hydrogen binding with Gibbs free energy changes (ΔG_{H^*}) ranging from 1.937 eV to 2.371 eV—far from the thermoneutral value (≈0 eV) required for efficient HER catalysis. This poor intrinsic activity stems from the fully coordinated surface atoms that lack the electronic flexibility necessary for optimal hydrogen adsorption and desorption, creating a critical bottleneck that prevents these materials from realizing their photocatalytic potential. To address this fundamental challenge, we systematically investigate how metal vacancy introduction can transform the catalytic landscape by creating undercoordinated active sites with modified electronic environments that facilitate efficient hydrogen evolution while preserving the beneficial Janus charge separation properties.

Strategic metal vacancy engineering dramatically transforms the HER activity through localized electronic structure modification and creation of highly reactive coordination-unsaturated sites. Fig. 4 demonstrates this remarkable transformation, while pristine surfaces show uniformly poor hydrogen binding (Fig. 4a), vacancy introduction reduces ΔG_{H^*} values to a competitive range of −0.371 eV to +0.607 eV (Fig. 4b). The most active configurations emerge from Ga/In vacancy formation, particularly in selenium-containing systems where $AlGaSe_2$@GaV achieves ΔG_{H^*} = −0.221 eV and $AlInSe_2$@InV reaches ΔG_{H^*} = −0.371 eV, approaching optimal thermoneutral conditions. These dramatic improvements – representing energy reductions exceeding 2 eV compared to pristine surfaces – arise from vacancy-induced creation of undercoordinated chalcogen atoms with enhanced reactivity due to unsaturated dangling bonds and localized electronic states within the band gap that facilitate efficient charge transfer to adsorbed hydrogen intermediates.

Systematic structure–activity analysis reveals clear design principles, Ga/In vacancies consistently outperform Al vacancies due to their larger atomic radii creating more significant structural distortion and electronic perturbation, while selenium-containing systems achieve optimal performance by balancing hydrogen binding strength with activation energy requirements. Benchmarking against established 2D catalysts positions these defect-engineered systems competitively within the broader materials landscape—dramatically outperforming pristine graphene (ΔG_H = 1.81–1.90 eV) [41] and the inactive basal plane of MoS_2 (ΔG_H = 1.4–2.2 eV) [42,43], while approaching the activity of MoS_2 edge sites (ΔG_H = 0.08–0.2 eV) and optimized borophene phases (ΔG_H ≈ 0.02 eV) [44]. Most significantly, the best-performing defect-engineered compositions rival the benchmark Pt(111) catalyst (ΔG_H ≈ 0.09 eV) [45], demonstrating that rational defect engineering can achieve noble metal-comparable HER activity while maintaining the advantages of earth-abundant materials, cost-effectiveness, and seamless integration with the inherent photocatalytic charge separation properties of Janus structures.

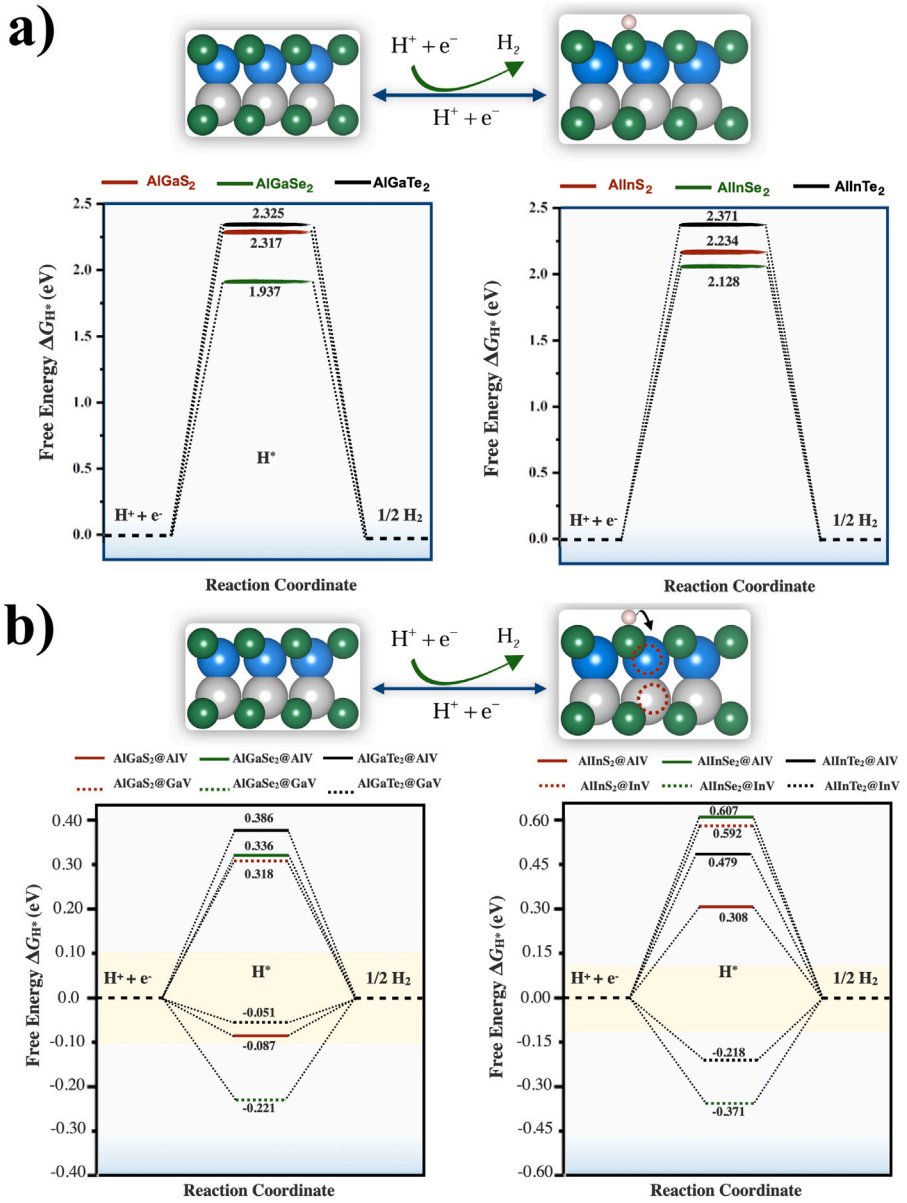

Fig. 4. Defect-Mediated Hydrogen Evolution in 2D Janus $AlXY_2$ Monolayers. Al, X (Ga, In) and Y (S, Se, Te) are in blue, gray and green colors respectively. (a) Free energy profiles for HER on $AlGaS_2$, $AlGaSe_2$, $AlGaTe_2$, $AlInS_2$, $AlInSe_2$, and $AlInTe_2$. (b) Free energy diagrams with defects, where @AlV denotes Al vacancies, @GaV denotes Ga vacancies, and @InV denotes In vacancies, showing the Gibbs free energy change (ΔG_{H^*}) for the H* intermediate.

3. Conclusions

This comprehensive first-principles investigation establishes 2D Janus $AlXY_2$ monolayers (X = Ga, In; Y = S, Se, Te) as a promising new class of photocatalysts for hydrogen evolution, demonstrating how asymmetric structural design can overcome fundamental limitations in conventional 2D materials. All six systems exhibit exceptional structural, dynamic, and thermal stability combined with suitable band gaps (2.029–2.969 eV) and intrinsic electric fields (5.391–6.437 V) that effectively suppress charge recombination—a critical advantage for photocatalytic applications. While pristine surfaces show poor HER activity (ΔG_{H^*} = 1.937–2.371 eV), strategic defect engineering through metal vacancy introduction transforms these materials into highly active electrocatalysts, with $AlInSe_2$@InV achieving ΔG_{H^*} = −0.371 eV that approaches the performance of noble metal catalysts. The combination of built-in charge separation, earth-abundant composition, and defect-tunable catalytic activity positions these Janus materials as compelling candidates for sustainable hydrogen production, offering a rational design framework for developing next-generation photocatalysts that simultaneously address the challenges of light harvesting, charge transport, and surface reactivity in a single material platform.

4. Computational methods

All first-principles calculations were performed using density functional theory (DFT) as implemented in the Vienna Ab Initio Simulation Package (VASP) [46]. Structural optimizations and total energy calculations employed the Perdew–Burke–Ernzerhof (PBE) functional within the generalized gradient approximation (GGA) [47], while electronic properties and band gap calculations utilized the Heyd–Scuseria–Ernzerhof (HSE06) hybrid functional with 25% exact exchange mixing [48] to correct the well-known DFT underestimation of semiconductor band gaps. A plane-wave basis set with a kinetic energy cutoff of 600 eV was employed, ensuring convergence of total energies to within 1 meV per atom. Geometry optimizations were performed with stringent convergence criteria of 10^{-6} eV for total energy and

10^{-4} eV/Å for atomic forces. To eliminate spurious interactions between periodic images, a vacuum layer of 20 Å was introduced along the c-direction, and Brillouin zone sampling was performed using a high-density 24 × 24 × 1 Monkhorst–Pack k-point grid [49]. Charge transfer analysis was conducted using the Bader charge partitioning algorithm [50].

Structural stability was rigorously assessed through multiple complementary approaches. Thermodynamic stability was evaluated via formation energy calculations using total energies of the optimized $AlXY_2$ monolayers and isolated constituent atoms. Dynamic stability was confirmed through phonon dispersion calculations using the finite displacement method as implemented in the Phonopy package [51–53], ensuring the absence of imaginary frequencies throughout the Brillouin zone. Thermal stability was validated through extensive ab initio molecular dynamics (AIMD) simulations using 5 × 5 × 1 supercells containing 100 atoms for each $AlXY_2$ system. The simulations employed the canonical (NVT) ensemble with a Nosé-Hoover thermostat (time constant of 0.5 fs) and 1 fs timesteps over 10 ps duration at temperatures of 300 K and 600 K to assess stability under ambient and elevated temperature conditions [54,55].

Hydrogen evolution reaction (HER) calculations employed 2 × 2 × 1 supercells (16 atoms) to minimize artificial hydrogen–hydrogen interactions, while defect studies utilized larger 4 × 4 × 1 supercells with single metal atom removal, corresponding to a vacancy concentration of approximately 1.56%. The hydrogen adsorption energy was calculated as:

$$\Delta E_{H^*} = E(\mathrm{AlXY_2} + H) - E(\mathrm{AlXY_2}) - \frac{1}{2}E(H_2) \tag{2}$$

where $E(\mathrm{AlXY_2}+H)$ represents the total energy of the $AlXY_2$ monolayer with an adsorbed hydrogen atom, $E(\mathrm{AlXY_2})$ is the total energy of the pristine monolayer, and $E(H_2)$ is the total energy of an isolated hydrogen molecule.

The Gibbs free energy of hydrogen adsorption, which determines HER activity, was computed incorporating temperature-dependent corrections [42,56]:

$$\Delta G_{H^*} = \Delta E_{H^*} + \Delta \mathrm{ZPE} - T\Delta S \tag{3}$$

where ΔZPE represents the zero-point energy difference, T is the temperature (298.15 K), and ΔS is the entropy change upon hydrogen adsorption. Following established protocols for hydrogen adsorption thermodynamics on metal surfaces [57], the entropic contribution ($T\Delta S$) and zero-point energy correction (ΔZPE) approximately cancel, yielding the commonly used approximation:

$$\Delta G_{H^*} = \Delta E_{H^*} + 0.24\,\mathrm{eV} \tag{4}$$

Vacancy defects were modeled by removing individual metal atoms (Al, Ga, or In) from 4 × 4 × 1 supercells, with defect formation energies calculated as [58,59]:

$$E_{\mathrm{form}} = E(\mathrm{defect}) - E(\mathrm{perfect}) + \mu_{\mathrm{metal}} \tag{5}$$

where E(defect) and E(perfect) are the total energies of the defective and pristine systems, respectively, and μ_{metal} represents the chemical potential of the removed metal atom referenced to its bulk metallic phase.

Band edge alignments were determined through rigorous electrostatic potential analysis, with absolute band positions calculated by aligning the electrostatic potential in the vacuum region with the computed eigenvalues. The electrostatic potential difference across the monolayer ($\Delta\phi$), which quantifies the strength of the intrinsic electric field arising from Janus asymmetry, was computed as the difference between asymptotic electrostatic potentials on opposite surfaces of the slab model.

CRediT authorship contribution statement

Talha Zafer: Writing – original draft, Visualization, Validation, Software, Methodology, Investigation, Formal analysis, Data curation, Conceptualization. **Nabil Khossossi:** Writing – review & editing, Validation, Supervision, Methodology, Formal analysis. **Poulumi Dey:** Writing – review & editing, Software, Project administration.

Declaration of competing interest

The authors declare that they have no known competing financial interests or personal relationships that could have appeared to influence the work reported in this paper.

Acknowledgments

This work was facilitated by NWO Domain Science for the use of supercomputer facilities. The authors also acknowledge the use of Delft-Blue supercomputer, provided by Delft High Performance Computing Center.

Appendix A. Supplementary data

Supplementary material related to this article can be found online at https://doi.org/10.1016/j.apsadv.2025.100851. Supporting electronic information is available.

Data availability

Data will be made available on request.

References

[1] R.J. Pearson, M.D. Eisaman, J.W. Turner, P.P. Edwards, Z. Jiang, V.L. Kuznetsov, K.A. Littau, L. di Marco, S.G. Taylor, Energy storage via carbon-neutral fuels made from CO2, water, and renewable energy, Proc. IEEE 100 (2012) 440–460, http://dx.doi.org/10.1109/JPROC.2011.2168369.

[2] X. Chen, C. Li, M. Grätzel, R. Kostecki, S.S. Mao, Nanomaterials for renewable energy production and storage, Chem. Soc. Rev. 41 (2012) 7909–7937, http://dx.doi.org/10.1039/C2CS35230C.

[3] N.Z. Muradov, T.N. Veziroğlu, "Green" path from fossil-based to hydrogen economy: An overview of carbon-neutral technologies, Int. J. Hydrog. Energy 33 (2008) 6804–6839, http://dx.doi.org/10.1016/j.ijhydene.2008.08.054.

[4] J. Zhu, L. Hu, P. Zhao, L.Y.S. Lee, K.-Y. Wong, Recent advances in electrocatalytic hydrogen evolution using nanoparticles, Chem. Rev. 120 (2020) 851–918, http://dx.doi.org/10.1021/acs.chemrev.9b00248.

[5] P. Kumar, R. Boukherroub, K. Shankar, Sunlight-driven water-splitting using two-dimensional carbon based semiconductors, J. Mater. Chem. A 6 (27) (2018) 12876–12931.

[6] M.G. Walter, E.L. Warren, J.R. McKone, S.W. Boettcher, Q. Mi, E.A. Santori, N.S. Lewis, Solar water splitting cells, Chem. Rev. 110 (2010) 6446–6473, http://dx.doi.org/10.1021/cr1002326.

[7] A.K. Singh, K. Mathew, H.L. Zhuang, R.G. Hennig, Computational screening of 2D materials for photocatalysis, J. Phys. Chem. Lett. 6 (2015) 1087–1098, http://dx.doi.org/10.1021/jz502646d.

[8] C.-F. Fu, X. Wu, J. Yang, Material design for photocatalytic water splitting from a theoretical perspective, Adv. Mater. 30 (2018) 1802106, http://dx.doi.org/10.1002/adma.201802106.

[9] J.R. Bolton, S.J. Strickler, J.S. Connolly, Limiting and realizable efficiencies of solar photolysis of water, Nature 316 (1985) 495–500, http://dx.doi.org/10.1038/316495a0.

[10] Y. Qu, X. Duan, Progress, challenge and perspective of heterogeneous photocatalysts, Chem. Soc. Rev. 42 (2013) 2568–2580, http://dx.doi.org/10.1039/C2CS35355E.

[11] M. Jakhar, A. Kumar, P.K. Ahluwalia, K. Tankeshwar, R. Pandey, Engineering 2D materials for photocatalytic water-splitting from a theoretical perspective, Materials 15 (2022) 2221, http://dx.doi.org/10.3390/ma15062221.

[12] N.N. Rosman, R.M. Yunus, L.J. Minggu, K. Arifin, M.N.I. Salehmin, M.A. Mohamed, M.B. Kassim, Photocatalytic properties of two-dimensional graphene and layered transition-metal dichalcogenides based photocatalyst for photoelectrochemical hydrogen generation: an overview, Int. J. Hydrog. Energy 43 (41) (2018) 18925–18945.

[13] U. Gupta, C. Rao, Hydrogen generation by water splitting using MoS2 and other transition metal dichalcogenides, Nano Energy 41 (2017) 49–65.

[14] M. Faraji, M. Yousefi, S. Yousefzadeh, M. Zirak, N. Naseri, T.H. Jeon, W. Choi, A.Z. Moshfegh, Two-dimensional materials in semiconductor photoelectrocatalytic systems for water splitting, Energy & Environ. Sci. 12 (1) (2019) 59–95.

[15] Y.H.R. Chang, K. Yao, K.H. Yeoh, M. Yoshiya, J. Jiang, M.H. Tuh, H.Y. Khong, T.L. Lim, Strain-induced SiP–PtS2 heterostructure with fast carrier transport for boosted photocatalytic hydrogen conversion, J. Phys. Chem. C 127 (26) (2023) 12760–12769, http://dx.doi.org/10.1021/acs.jpcc.3c02431.

[16] Y.H.R. Chang, K.H. Yeoh, J. Jiang, S.S. Chai, Q. Liang, M.H. Tuh, S.H. Leong, T.L. Lim, L.C. Low, Y.S. Yong, Activating the screened thermoelectric and photocatalytic water-splitting potential in janus Sn2XY (X, Y=Te, Se, and S) monolayers via doping and strain engineering, J. Phys. Chem. C 129 (3) (2025) 1885–1896, http://dx.doi.org/10.1021/acs.jpcc.4c06561.

[17] K. Maeda, K. Domen, Photocatalytic water splitting: Recent progress and future challenges, J. Phys. Chem. Lett. 1 (2010) 2655–2661, http://dx.doi.org/10.1021/jz1007966.

[18] C.-F. Fu, J. Sun, Q. Luo, X. Li, W. Hu, J. Yang, Intrinsic electric fields in two-dimensional materials boost the solar-to-hydrogen efficiency for photocatalytic water splitting, Nano Lett. 18 (10) (2018) 6312–6317.

[19] X. Li, Z. Li, J. Yang, Proposed photosynthesis method for producing hydrogen from dissociated water molecules using incident near-infrared light, Phys. Rev. Lett. 112 (2014) 018301, http://dx.doi.org/10.1103/PhysRevLett.112.018301.

[20] Z. Haman, N. Khossossi, M. Kibbou, I. Bouziani, D. Singh, I. Essaoudi, A. Ainane, R. Ahuja, Janus aluminum oxysulfide Al2OS: A promising 2D direct semiconductor photocatalyst with strong visible light harvesting, Appl. Surf. Sci. 589 (2022) 152997, http://dx.doi.org/10.1016/j.apsusc.2022.152997.

[21] G. Liu, J. Peng, B. Jia, J. Hao, Z. Zhao, X. Ma, W. Zou, P. Lu, Catalytic activity for hydrogen evolution reaction of Janus monolayer MoXTe (X=S, Se), Int. J. Hydrog. Energy 48 (37) (2023) 13902–13912.

[22] L. Ju, X. Tang, J. Li, L. Shi, D. Yuan, Breaking the out-of-plane symmetry of Janus WSSe bilayer with chalcogen substitution for enhanced photocatalytic overall water-splitting, Appl. Surf. Sci. 574 (2022) 151692.

[23] A.Y. Lu, H. Zhu, J. Xiao, C.P. Chuu, Y. Han, M.H. Chiu, C.C. Cheng, C.W. Yang, K.H. Wei, Y. Yang, Y. Wang, D. Sokaras, D. Nordlund, P. Yang, D.A. Muller, M.Y. Chou, X. Zhang, L.J. Li, Janus monolayers of transition metal dichalcogenides, Nature Nanotechnology 12 (2017) 744–749, http://dx.doi.org/10.1038/nnano.2017.100.

[24] L. Ju, M. Bie, X. Tang, J. Shang, L. Kou, Janus WSSe monolayer: an excellent photocatalyst for overall water splitting, ACS Appl. Mater. & Interfaces 12 (26) (2020) 29335–29343.

[25] D. Ge, R. Luo, X. Wang, L. Yang, W. Xiong, F. Wang, Internal and external electric field tunable electronic structures for photocatalytic water splitting: Janus transition-metal chalcogenides/C3N4 van der Waals heterojunctions, Appl. Surf. Sci. 566 (2021) 150639, http://dx.doi.org/10.1016/j.apsusc.2021.150639.

[26] Z. Haman, M. Kibbou, N. Khossossi, S. Bahti, P. Dey, I. Essaoudi, R. Ahuja, A. Ainane, Photocatalytic and thermoelectric performance of asymmetrical two-dimensional Janus aluminium chalcogenides, J. Phys.: Energy 5 (2023) 035008, http://dx.doi.org/10.1088/2515-7655/ace07c.

[27] P. Jamdagni, A. Kumar, S. Srivastava, R. Pandey, K. Tankeshwar, Photocatalytic properties of anisotropic β-PtX 2 (X=S, Se) and Janus β-PtSSe monolayers, Phys. Chem. Chem. Phys. 24 (36) (2022) 22289–22297.

[28] P. Chauhan, J. Singh, A. Kumar, As-based ternary Janus monolayers for efficient thermoelectric and photocatalytic applications, J. Mater. Chem. A 11 (19) (2023) 10413–10424.

[29] P. Zhao, Y. Ma, X. Lv, M. Li, B. Huang, Y. Dai, Two-dimensional III2-VI3 materials: Promising photocatalysts for overall water splitting under infrared light spectrum, Nano Energy 51 (2018) 533–538.

[30] Y. Fan, X. Ma, J. Wang, X. Song, A. Wang, H. Liu, M. Zhao, Highly-efficient overall water splitting in 2D Janus group-III chalcogenide multilayers: the roles of intrinsic electric filed and vacancy defects, Sci. Bull. 65 (1) (2020) 27–34.

[31] J.-H. Yuan, K.-H. Xue, X. Miao, Two-dimensional ABC3 (A=Sc, Y; B=Al, Ga, In; C=S, Se, Te) with intrinsic electric field for photocatalytic water splitting, Int. J. Hydrog. Energy 48 (15) (2023) 5929–5939.

[32] C. Wan, H. An, C. Liu, L. Meng, W. Yan, X. Yan, Janus XYZ2 (X/Y=Al, Ga, and In; X≠ Y; Z=S, Se, and Te) monolayers: Excellent photocatalysts for water splitting, Chem. Phys. 595 (2025) 112714.

[33] D. Oxtoby, H. Gillis, A. Campion, Principles of Modern Chemistry, Cengage Learning, ISBN: 9780840049315, 2011.

[34] D. Alfè, PHON: A program to calculate phonons using the small displacement method, Comput. Phys. Comm. (ISSN: 0010-4655) 180 (12) (2009) 2622–2633, 40 YEARS OF CPC: A celebratory issue focused on quality software for high performance, grid and novel computing architectures. http://dx.doi.org/10.1016/j.cpc.2009.03.010, URL https://www.sciencedirect.com/science/article/pii/S0010465509001064.

[35] W. Wan, S. Zhao, Y. Ge, Y. Liu, Phonon and electron transport in Janus monolayers based on InSe, J. Phys.: Condens. Matter. 31 (43) (2019) 435501, http://dx.doi.org/10.1088/1361-648X/AB2E7D.

[36] M.V. Fischetti, W.G. Vandenberghe, Mermin-Wagner theorem, flexural modes, and degraded carrier mobility in two-dimensional crystals with broken horizontal mirror symmetry, Phys. Rev. B 93 (15) (2016) 155413, http://dx.doi.org/10.1103/PHYSREVB.93.155413.

[37] B. Zhang, L. Zhang, N. Yang, X. Zhao, C. Chen, Y. Cheng, I. Rasheed, L. Ma, J. Zhang, 2D Young's modulus of black phosphorene with different layers, J. Phys. Chem. C 126 (2) (2022) 1094–1098.

[38] J.-W. Jiang, J.-S. Wang, B. Li, Young's modulus of graphene: A molecular dynamics study, Phys. Rev. B 80 (2009) 113405, http://dx.doi.org/10.1103/PhysRevB.80.113405, URL https://link.aps.org/doi/10.1103/PhysRevB.80.113405.

[39] L. Wei, C. Jun-fang, H. Qinyu, W. Teng, Electronic and elastic properties of MoS2, Phys. B 405 (10) (2010) 2498–2502.

[40] Y. Zhu, X. Cao, Y. Tan, Y. Wang, J.Q. Hu, B. Li, Z. Chen, Single-layer MoS_2: A two-dimensional material with negative Poisson's ratio, Coatings 13 (2) (2023) 283, http://dx.doi.org/10.3390/coatings13020283.

[41] C.L. Bentley, M. Kang, F.M. Maddar, F. Li, M. Walker, J. Zhang, P.R. Unwin, Electrochemical maps and movies of the hydrogen evolution reaction on natural crystals of molybdenite (MoS2): basal vs. edge plane activity, Chem. Sci. 8 (2017) 6583–6593, http://dx.doi.org/10.1039/C7SC02545A.

[42] B. Hinnemann, P.G. Moses, J. Bonde, K.P. Jørgensen, J.H. Nielsen, S. Horch, I. Chorkendorff, J.K. Nørskov, Biomimetic hydrogen evolution: MoS2 nanoparticles as catalyst for hydrogen evolution, J. Am. Chem. Soc. 127 (15) (2005) 5308–5309, PMID: 15826154. http://dx.doi.org/10.1021/ja0504690.

[43] T.F. Jaramillo, K.P. Jørgensen, J. Bonde, J.H. Nielsen, S. Horch, I. Chorkendorff, Identification of active edge sites for electrochemical H₂ evolution from MoS₂ nanocatalysts, Science 317 (5834) (2007) 100–102, http://dx.doi.org/10.1126/science.1141483, URL https://www.science.org/doi/abs/10.1126/science.1141483.

[44] E.E. Siddharthan, S. Ghosh, R. Thapa, Bond exchange mechanism: Unveiling the volmer–tafel pathway and an electronic descriptor for predicting hydrogen evolution reaction activity of borophene, ACS Appl. Energy Mater. 6 (17) (2023) 8941–8948, http://dx.doi.org/10.1021/acsaem.3c01570.

[45] E. Skúlason, G.S. Karlberg, J. Rossmeisl, T. Bligaard, J. Greeley, H. Jónsson, J.K. Nørskov, Density functional theory calculations for the hydrogen evolution reaction in an electrochemical double layer on the Pt(111) electrode, Phys. Chem. Chem. Phys. 9 (2007) 3241–3250, http://dx.doi.org/10.1039/B700099E.

[46] G. Kresse, J. Furthmüller, Efficient iterative schemes for ab initio total-energy calculations using a plane-wave basis set, Phys. Rev. B 54 (1996) 11169–11186, http://dx.doi.org/10.1103/PhysRevB.54.11169.

[47] J.P. Perdew, K. Burke, M. Ernzerhof, Generalized gradient approximation made simple, Phys. Rev. Lett. 77 (1996) 3865–3868, http://dx.doi.org/10.1103/PhysRevLett.77.3865.

[48] J. Heyd, G.E. Scuseria, M. Ernzerhof, Hybrid functionals based on a screened Coulomb potential, J. Chem. Phys. 118 (2003) 8207–8215, http://dx.doi.org/10.1063/1.1564060.

[49] H.J. Monkhorst, J.D. Pack, Special points for Brillouin-zone integrations, Phys. Rev. B 13 (1976) 5188–5192, http://dx.doi.org/10.1103/PhysRevB.13.5188.

[50] G. Henkelman, A. Arnaldsson, H. Jónsson, A fast and robust algorithm for bader decomposition of charge density, Comput. Mater. Sci. 36 (2006) 354–360, http://dx.doi.org/10.1016/j.commatsci.2005.04.010.

[51] L. Chaput, A. Togo, I. Tanaka, G. Hug, Phonon-phonon interactions in transition metals, Phys. Rev. B 84 (2011) 094302, http://dx.doi.org/10.1103/PhysRevB.84.094302.

[52] K. Parlinski, Z.Q. Li, Y. Kawazoe, First-principles determination of the soft mode in cubic ZrO2, Phys. Rev. Lett. 78 (1997) 4063–4066, http://dx.doi.org/10.1103/PhysRevLett.78.4063.

[53] A. Togo, F. Oba, I. Tanaka, First-principles calculations of the ferroelastic transition between rutile-type and CaCl2-type SiO2 at high pressures, Phys. Rev. B 78 (2008) 134106, http://dx.doi.org/10.1103/PhysRevB.78.134106.

[54] M. Parrinello, A. Rahman, Crystal structure and pair potentials: A molecular-dynamics study, Phys. Rev. Lett. 45 (1980) 1196–1199, http://dx.doi.org/10.1103/PhysRevLett.45.1196.

[55] L. Kantorovich, N. Rompotis, Generalized Langevin equation for solids. II. Stochastic boundary conditions for nonequilibrium molecular dynamics simulations, Phys. Rev. B 78 (2008) 094305, http://dx.doi.org/10.1103/PhysRevB.78.094305.

[56] J.K. Nørskov, et al., Trends in the exchange current for hydrogen evolution, J. Electrochem. Soc. 152 (2005) J23–J26, http://dx.doi.org/10.1149/1.1856988.

[57] A. Govender, D. Curulla Ferré, J.W.H. Niemantsverdriet, A density functional theory study on the effect of zero-point energy corrections on the methanation profile on Fe(100), ChemPhysChem 13 (6) (2012) 1591–1596, http://dx.doi.org/10.1002/cphc.201100733, URL https://chemistry-europe.onlinelibrary.wiley.com/doi/abs/10.1002/cphc.201100733.

[58] C.G. Van de Walle, J. Neugebauer, First-principles calculations for defects and impurities: Applications to III-nitrides, J. Appl. Phys. 95 (2004) 3851–3879, http://dx.doi.org/10.1063/1.1682673.

[59] S. Lany, A. Zunger, Accurate prediction of defect properties in density functional supercell calculations, Modelling Simul. Mater. Sci. Eng. 17 (2009) 084002, http://dx.doi.org/10.1088/0965-0393/17/8/084002.